Title

Preference of CAMSAP3 for microtubules with expanded lattice contributes to stabilization of the minus end

Author

Hanjin Liu, Tomohiro Shima[#]

Affiliation

Department of Biological Sciences, Graduate School of Science, The University of Tokyo

Hongo 7-3-1, Bunkyo-ku, Tokyo #113-0033, JAPAN

Corresponding author

T. S. Tel: +81 (0) 3 5841 4399, Email: tomohiro.shima@bs.s.u-tokyo.ac.jp

Abstract

CAMSAPs are proteins that characteristically show microtubule minus-end-specific localization, decoration and stabilization. Although the mechanism for minus-end recognition via their C-terminal CKK domain has been well described in recent structural studies, it is unclear how CAMSAPs stabilize microtubules and why the stabilizing effect varies among the three family members, CAMSAP1, 2 and 3. We conducted several binding assays under fluorescence microscopy and revealed that D2, the helical region of CAMSAP3 next to the CKK domain, specifically binds to microtubules with the expanded lattice, such as GMPCPP-polymerized, taxol-stabilized and kinesin-pretreated microtubules. To investigate the relationship between this preference and the stabilization effect of CAMSAP3, we precisely measured individual microtubule lengths and found that D2-binding expanded the microtubule lattice by ~3%. Consistent with the notion that the expanded lattice is a common feature of stable microtubules, the presence of D2 slowed the microtubule depolymerization rate to approximately 1/20, suggesting that the D2-triggered lattice expansion stabilizes microtubules. Combining these results, we propose that CAMSAP3 stabilizes microtubules in two steps: first, by recruitment to the microtubule minus end via the CKK domain, and then by lattice expansion upon D2-binding to stabilize the microtubule and accelerate the recruitment of other CAMSAP3 molecules. Since only CAMSAP3 has D2 and the highest microtubule stabilizing effect among mammalian CAMSAPs, our model also explains the molecular basis for the functional diversity of CAMSAP family members.

Introduction

Microtubules are a eukaryotic cytoskeleton with a hollow cylindric structure composed of α- and β-tubulin heterodimers (Zhang *et al*., 2018). They play essential cellular roles such as providing mechanical strength, building the machinery for cell division and working as the railway on which motor proteins transport intracellular components (Dent *et al*., 2014; Goodson and Jonasson, 2018). Microtubules change their spatio-temporal distributions in cells in response to biochemical signals to construct the basic machinery for mitosis, cellular development and migration (Gadde and Heald 2004; Williamson *et al*., 1996; Dogterom and Koenderink, 2019). This dynamic reorganization is achieved mainly by two phenomena: polymerization/depolymerization and nucleation. Polymerization and depolymerization refer to the addition/removal of tubulin dimers at pre-existing microtubule tips, which results in microtubule elongation and shrinkage, respectively, a phenomenon usually called dynamic instability (Mitchison and Kirschner, 1984). On the other hand, microtubule nucleation generates new microtubules from tubulin dimers (Job *et al*., 2003; Ayukawa *et al*., 2021). Fine regulation of dynamic instability and nucleation is important for keeping microtubule networks ordered in cells and thus for proper cell activities.

Eukaryotes have a huge number of microtubule-associated proteins (MAPs) that alter microtubule dynamics. For instance, microtubule end-tracking proteins EB1 and XMAP215 increase the microtubule growth rate and catastrophe frequency, promoting microtubule dynamic instability (Zanic *et al*., 2013; Farmer *et al*., 2021), whereas cytoplasmic linker-associated proteins (CLASPs) protect microtubules from depolymerization and suppress catastrophe (Aher *et al*., 2018). Among MAPs, calmodulin-regulated spectrin-associated proteins (CAMSAPs) and the invertebrate homolog patronin track the microtubule minus end and regulate microtubule dynamics (Hendershott *et al*., 2014; Jiang *et al*., 2014; Akhmanova and Steinmetz, 2019). Patronin/CAMSAPs are also hypothesized to be non-centrosomal microtubule nucleators, thus providing an indispensable role in cells that need microtubules to be nucleated far from the cell centrosome (Meng *et al*., 2008; Goodwin and Vale, 2010; Tanaka *et al*., 2012; Feng *et al*., 2019; Imasaki et al., 2022). In cells, mutations or knockdown of CAMSAPs disturb microtubule growth or patterning, reaffirming the importance of these proteins in microtubule organization (Tanaka *et al*., 2012; Toya *et al*., 2016; Pongrakhananon *et al*., 2018; Coquand *et al*., 2021).

Vertebrates generally have three CAMSAP members, CAMSAP1-3, which show slight differences in their interactions and functions with microtubules. *In vitro* experiments using mouse CAMSAPs found that CAMSAP1 can track the microtubule minus tip but does not affect microtubule dynamics. On the other hand, CAMSAP2 not only tracks the microtubule minus tip but remains bound to the microtubule after minus end elongation, resulting in microtubule decoration at the larger area of minus ends. It also stabilizes microtubules and protects microtubules from catastrophe. Finally, CAMSAP3 decorates and stabilizes microtubule minus ends, with a stronger effect than CAMSAP2. CAMSAPs consist of several coiled-coil regions and a well-conserved C-terminal globular domain called CKK (Atherton *et al*., 2017) that is responsible for the minus-end specificity of the proteins. Recent structural studies on the CKK domain have revealed how the CKK domain recognizes slight structural differences between microtubule minus ends and other regions (Atherton *et al*.,

2017; Atherton *et al*., 2019). However, these studies investigated the CKK domain only and failed to clarify the mechanism of the microtubule stabilization by CAMSAP2/3 and why CAMSAP1 does not have this property.

To understand the microtubule stabilization mechanism, it is necessary to consider the structure of not only CAMSAPs but of microtubules too. Recent cryogenic electron microscopy (cryo-EM), X-ray diffraction and fluorescence microscopy studies have shown that microtubules can take diverse conformations depending on their binding states with nucleotides, proteins and chemical agents. In terms of microtubule stability, the lattice expansion/compaction of the tubulin periodicity along the longitudinal axis shows a clear correlation. The inhibition of microtubule depolymerization by the very slowly hydrolysable nucleotide guanosine-5'-[(α, β)-methyleno]triphosphate (GMPCPP), treatment with the anti-cancer drug taxol (Alushin *et al.*, 2014; Kamimura *et al.*, 2016) or mutations in the GTPase site (LaFrance *et al.*, 2022) forces microtubules to take conformations with the expanded lattice compared to the unstable GDP-bound state. Therefore, lattice expansion is thought to be a common conformational change needed for microtubule stabilization.

The lattice expansion/compaction provides a flexible way to control microtubule stability and is recognized by MAPs. The cell division master regulator TPX2 (Roostalu *et al.*, 2015) and motor protein KIF5C (Nakata *et al.*, 2011; Morikawa *et al.*, 2015) can "read" the differences in microtubule conformations and preferentially bind to the expanded lattice. Interestingly, more recent studies have shown that both TPX2 and KIF5C actively introduce lattice expansion to compact microtubules or, in other words, "write" structural code on the microtubule and stabilize it upon their binding (Zhang *et al.*, 2017; Shima *et al.*, 2018; Peet *et al.*, 2018). Considering the "reading" and "writing" abilities are conferred to KIF5C and TPX2 in a conjugative manner, it may be common for "reader" proteins to work as "writers" as well and stabilize microtubules through lattice expansion. Because preferential binding to the expanded lattice implies that the expanded lattice is energetically favorable for the "reader"-microtubule complex, this difference in free energy may be the driving force that expands the compact lattice.

The discovery of "reader/writer" MAPs raises the possibility that a similar "reader/writer" region exists in CAMSAP2/3 but not CAMSAP1. Truncation studies of CAMSAPs have demonstrated that CAMSAP2/3 have regions that, unlike the CKK domain, bind to the expanded lattice of GMPCPP-stabilized microtubule seeds but hardly bind to the compact lattice of dynamically polymerized GDP-bound microtubules (Jiang *et al*., 2014; Atherton *et al*., 2017). These truncated constructs have included the middle region, named microtubule binding domain (MBD), or region adjacent to the CKK domain, named D2, for which little is known (see Fig. S1 of Atherton *et al*., 2017). Because these regions seem to "read" the expanded lattice, we hypothesized they play a key role in stabilizing microtubules.

Here, we investigated the D2 region, which has 139 residues, of human CAMSAP3 for its contribution to microtubule stabilization. Our series of *in vitro* experiments revealed that D2 has high affinity for various types of microtubules with the expanded lattice, including GMPCPP-stabilized, taxol-stabilized and KIF5C-pretreated GDP-microtubules. Consistent with our hypothesis, an excess amount of D2 expanded the lattice of GDP-microtubules and inhibited depolymerization. These results strongly suggest that D2 shares similar lattice "reader/writer" abilities with KIF5C and, therefore, can regulate microtubule dynamics upon its binding. The

synergy between the properties of D2 and the minus-end tracking ability of the CKK domain provides a common explanation for the complex physiological roles of CAMSAPs.

3. Results

D2 region of human CAMSAP3 preferentially binds to GMPCPP-stabilized microtubules.

Previous *in vitro* microtubule dynamics assays have shown that the D2 region of mouse CAMSAP3 decorates microtubule seeds (Atherton *et al*., 2017). Since the microtubule seeds were composed of GMPCPP-bound tubulin, these results implied that the D2 region has a preference for GMPCPP-stabilized microtubules over standard GDP-bound microtubules (polymerized with GTP and hydrolyzed to GDP).

To verify if the same microtubule preference also holds for our D2 construct from human CAMSAP3, we conducted the binding assay using non-dynamic microtubules under total internal reflection fluorescence (TIRF) microscopy. The D2 region conjugated with fluorescent protein mCherry (D2-mCherry) was expressed and purified from *E. coli* using a histidine tag (Fig. 1A; Fig. S1). GDP-bound microtubules (GDP-MT) were polymerized from GMPCPP-bound microtubules (GMPCPP-MT) immobilized on the glass surface by biotin/avidin conjugation (Fig. 1B). In our assay, we did not immobilize GMPCPP-MT and GDP-MT separately for two reasons. First, when microtubules are spontaneously nucleated without seeds, GMPCPP-MT mainly forms a 14-protofilament conformation, while GDP-MT takes 13- to 15-protofilament conformations (Hyman *et al.*, 1995). To eliminate the effect of the protofilament number, GDP-MT was polymerized from GMPCPP-MT. Second, to analyze the structural transition of the GDP-MT lattice, we needed to eliminate the direct immobilization of GDP-MT on the glass surface. The biotin/avidin immobilization may compete with and prevent the longitudinal expansion and/or skewing of the GDP-MT lattice. We avoided this problem by indirectly immobilizing GDP-MT via GMPCPP-MT. Thus, using this assay system, we observed D2-binding on GDP- and GMPCPP-MT. As expected, D2 specifically decorated GMPCPP-MT (Fig. 1C) but hardly bound to GDP-MT at D2 concentrations as high as 1 μM. Quantification of the fluorescence images showed exclusive binding on GMPCPP-MT at 0.25 μM D2 (GMPCPP-MT: 24 ± 6 a.u., GDP-MT: -0.6 ± 1.3 a.u.; mean ± S.D.) and 11-times higher affinity on GMPCPP-MT at 1 μM D2 (GMPCPP-MT: 78 ± 16 a.u., GDP-MT: 7.2 ± 4.9 a.u.; mean ± S.D.) (Fig. 1D). Thus, we confirmed that D2 prefers GMPCPP-MT and is a common feature of mouse and human CAMSAP3.

Affinity of D2 to microtubules increases in the presence of taxol

The preference of D2 to GMPCPP-MT is most likely due to the expanded lattice of GMPCPP-MT, in which the tubulin periodicity is expanded by 2-3% along the longitudinal axis compared to that of GDP-MT (Alushin *et al*., 2014). However, the different nucleotides in microtubules themselves (Estevez-Gallego et al., 2020) may also affect the affinity to D2. Therefore, we next investigated the affinity of D2 to other types of microtubules with expanded lattices. Taxol, a microtubule depolymerization inhibitor used as an anti-cancer drug, is known to expand microtubules and force microtubules to take a GMPCPP-bound-like structure (Yajima *et al*., 2012; Alushin *et al*., 2014; Kamimura *et al*., 2016). If the preference of D2 to GMPCPP-MT is attributed to the expanded lattice and not the interaction with the nucleotide itself, D2 should have a higher affinity for taxol-stabilized GDP-MT. To test this hypothesis, we conducted the same binding assay in the presence of 20 μM taxol, a concentration high enough to force microtubules to take the expanded lattice (Yajima *et al*., 2012). Indeed, the D2-mCherry intensity increased on both GDP- and GMPCPP-MT (Fig. 2A). Quantification revealed

that the intensity of D2-mCherry on GDP-MT increased from an undetectable level to 22 ± 6 a.u. at 250 nM D2, which is similar to the intensity of D2 bound to GMPCPP-MT without taxol (Fig. 2C). At 1 μM D2 with taxol, the amount D2 bound to GDP-MT reached 85% that bound to GMPCPP-MT. This value remained constant (86%) when the D2 concentration was elevated to 4 μM, implying that the preference of D2-binding reached a plateau at 1 μM. These results support the idea that D2 distinguishes expanded/compact lattices, not the nucleotide state of microtubules.

We also tested the reversibility of the effects of taxol using a taxol-depletion assay (Fig. 2B). In this assay, microtubules were first equilibrated with a solution containing D2 and taxol, and then taxol was subsequently depleted by exchanging the solution to D2 solution without taxol. Considering the fast dissociation (k_{off} ~30 s^{-1}; Caplow *et al*.,1994) and the weak affinity (K_d ~2 μM; Li *et al*., 2000; Ross *et al*., 2004) of taxol with GDP-MT, no more than ~1% of the bound taxol could remain bound or rebind during the incubation in taxol-free buffer. The presence of a stoichiometric amount of taxol is needed to expand the lattice (Kamimura et al., 2016). Therefore, after the taxol depletion, a subset of GDP-MTs was expected to take the compact lattice. At 1 μM or higher concentrations of D2-mCherry, the D2-mCherry fluorescence intensity on the MTs did not change after the taxol depletion (Fig. 2C). However, at a low D2 concentration (250 nM), D2 that used to be on the GDP-MT was partially dissociated after the taxol-depletion based on the significant decrease in intensity (Fig. 2C, Table 1). Furthermore, when we inspected individual microtubules, we found that D2 occasionally remained on GDP-MT as clusters (Fig. 2D). Line profiles along microtubules clearly showed a stepwise increase in mCherry intensity (Fig. 2E), which suggests that microtubules and/or D2 take distinct states in the cluster. Taken together, D2 recognizes the microtubule lattice expansion, and changes in the affinity between D2 and microtubules is reversible at low D2 concentrations.

D2 detects lattice expansion of native microtubules

TIRF microscopy showed that D2 affinity for microtubule positively correlates with the microtubule lattice expansion induced by GMPCPP or taxol. However, these chemical reagents do not exist in intact mammal cells. To confirm whether D2 can identify microtubule conformations in normal cells, we induced microtubule lattice expansion using a protein that is present in the cytoplasm. The microtubule motor protein KIF5C is known to trigger the transition of the GDP-MT lattice structure from the compacted to expanded state (Shima *et al*., 2018; Peet *et al*., 2018). Importantly, the microtubule lattice remains expanded for ~2 minutes after KIF5C dissociation is induced by a high ionic strength buffer (Shima *et al*., 2018), but it is immediately compacted (<4 seconds) when buffer containing ADP or AMPPNP is used instead (Peet *et al*., 2018, Shima *et al.*, 2018). Therefore, KIF5C treatment and washout are useful for modulating the lattice structure of native GDP-MT.

We repeated the KIF5C pre-treatment assay with several concentrations of KIF5C and washout buffers while keeping the D2 concentration constant at 1 μM (Fig. 3A). Compared to the case without KIF5C pre-treatment, the D2-binding affinity to GDP-MT significantly increased by pre-treatment with 0.1 μM KIF5C (Fig. 3B). Pre-treatment with higher concentrations of KIF5C further enhanced the D2 affinity for GDP-MT to almost the same level of that for GMPCPP-MT without the pre-treatment (Fig. 3B, C; Table 2). If D2 recognizes the lattice expansion induced by KIF5C, lattice compaction should lower the affinity between GDP-MT and D2

to the original weak state. Indeed, ADP-triggered lattice compaction upon KIF5C dissociation aborted D2-binding even at the highest KIF5C concentration tested (Fig. 3B, C). The mCherry intensity on GDP-MT did not drop to the original value ($p < 0.001$, Steel-Dwass test) but resembled the condition with 0.1 μM KIF5C pre-treatment. This incomplete rollback of the lattice structure may be due to the partial dissociation of D2, since ADP wash does not affect the binding of D2, which is a non-ATPase. To normalize the lattice structural deviation between conditions, we calculated the specificity of D2-binding by dividing the average mCherry intensity on GMPCPP-MT with that on GDP-MT (Fig. 3D). This analysis revealed that the specificity of D2 monotonically decreased in response to large amounts of KIF5C pretreatment and restored the specificity to the original state after the ADP wash. This observation too supports the notion that D2-binding is sensitive to microtubule lattice spacing.

D2 expands the microtubule lattice but the expansion is not meta-stable

Next, we speculated that the "reader" ability of D2 should also contribute to expand the lattice of GDP-MT when D2 excessively binds to it. To test this hypothesis, we conducted a microtubule expansion assay with a high concentration of D2 (Fig. 4A). We polymerized Cy5-labeled GDP-MT from Alexa Fluor 488-labeled GMPCPP seed and capped it with Alexa Fluor 488-labeled GMPCPP-MT to prevent depolymerization during the assay. Before adding D2, microtubules were straight along their entire length. With 4 μM D2, the microtubules were severely deformed despite extensive parallel flow during the buffer exchange (Fig. 4B). To precisely measure the microtubule length before and after D2-binding, we used a curve fitting algorithm on the fluorescence images. Microtubules were first fit to a two-dimensional (2D) B-spline Gaussian wall using the total fluorescence intensity. Subsequently, we measured the length of the Cy5-labeled region by a line scan of the Cy5 channel along the spline curve and fitting to the error function at both ends (see Methods). The presence of D2 caused a longitudinal elongation of GDP-MT that was associated with the lattice expansion. 4 μM D2 induced 3.1 ± 0.8% (mean ± S.D.) lattice expansion, which is comparable to TPX2/GMPCPP-induced double expansion (Zhang *et al*., 2018), the most expanded state to our knowledge (LaFrance *et al*., 2022).

As mentioned above, the lattice expansion induced by KIF5C lasts for ~2 min even after KIF5C dissociation by a high ionic strength buffer. Therefore, the KIF5C-triggered expanded lattice is assumed to be a meta-stable state (Shima *et al*., 2018). Since D2 expanded the lattice more than KIF5C did, the D2-induced expansion may last longer than that induced by KIF5C. To check the meta-stability of the D2-induced expanded lattice, D2 was washed out with the high ionic strength buffer after the lattice expansion, and the microtubule length was measured. Contrary to our expectation, the lattice compaction was completed within 90 seconds after the D2 dissociation (Fig. 4C). The results of the taxol-depletion assay (Fig. 2), in which D2 dissociated from a subset of the microtubule region immediately after taxol removal, also support the notion that insufficient amounts of bound D2 cause an immediate return of the expanded lattice to the compact state. Note that in the KIF5C pre-treatment assay (Fig. 3), the enhanced D2 affinity remained after KIF5C dissociation by the same buffer. Therefore, the lattice expansion triggered by D2 is reminiscent of that by KIF5C, but their effects are different in terms of stability against the compaction. Collectively, our expansion assay revealed that D2 can convert the

microtubule lattice into the expanded state, but the D2-triggered expanded state is not meta-stable so it returns to the compacted state immediately after the dissociation of D2.

D2-triggered expanded lattice is resistant to microtubule depolymerization

We revealed that D2-binding transforms microtubules to the expanded state. Although many types of microtubules with the expanded lattice are resistant to depolymerization, it is unclear if this is true for D2-induction. Therefore, we quantified the depolymerization rate by glycerol depletion with or without 4 μM D2 (Fig. 5A). A comparison of time lapse images in the absence (Fig. 5B) and presence of D2 (Fig. 5C) clearly indicated that depolymerization was strongly suppressed by 4 μM D2. Representative kymographs also showed an obvious difference between the two conditions (Fig. 5D, E). Before quantifying the depolymerization rate, we could not build kymographs for most microtubules, since microtubules changed their curves during depolymerization. As a workaround, we derived the depolymerization rate from the total fluorescence intensity in each specific region that surrounds individual microtubules throughout the imaging time (Fig. S3). We found that microtubule depolymerization dramatically slowed down from 0.82 ± 0.30 μm s^{-1} (mean ± S.D.) to 0.046 ± 0.028 μm s^{-1} upon exposure to 4 μM D2 (Fig. 5F). This result suggests that the lattice expansion by D2 protects microtubules from depolymerization.

4. Discussion

In this study, we demonstrated that the D2 region of human CAMSAP3 preferentially binds to the expanded lattice of microtubules. At saturating levels, D2 expanded the microtubule lattice by 3.1% (Fig. 4), which slowed the microtubule depolymerization rate down ~18 fold (Fig. 5). Combining these results with previously known functions of the CKK domain, we suggest a detailed model of microtubule stabilization by CAMSAP3 (Fig. 6A). The interaction between microtubules and CAMSAP3 is first formed via the CKK domain, since it occurs regardless of the presence of other CAMSAP3 domains (Jiang *et al*., 2014). Once a CAMSAP3 protein is bound to the microtubule surface, the local concentration of the D2 region at the minus end is dramatically increased. Assuming that the peptide between the microtubule binding region of D2 and the CKK domain (residues 1023-1111 for human CAMSAP3) takes the disordered conformation, which is predicted by AlphaFold2, and the inter-residue distance is 0.4 nm (Ainavarapu *et al.*, 2007), a D2 molecule would be confined to a volume of $4/3 \times \pi \times (0.4 \times 88)^3 = 9.1 \times 10^4$ nm^3 after CKK binding; thus, the D2 local concentration is estimated to be over 20 μM. Note that the local concentration is likely underestimated, since the peptide chain is unlikely to be tautly stretched due to entropic energy loss. Considering 4 μM D2 was sufficient to expand the lattice of GDP-MT (Fig. 4B), a local concentration over 20 μM should be high enough to convert the minus end into the expanded state with high affinity for D2. As a result, CAMSAP3 protein strongly interacts with the minus end of microtubules via divalent interactions of the CKK domain and D2 region, while the end is stabilized by the D2-induced lattice expansion (Fig. 5F). This expanded lattice recruits more CAMSAP3 molecules by promoting D2-microtubule interactions and prevents the dissociation of CAMSAP3. Previous work using recombinant CAMSAPs also supports the importance of non-CKK domains on the enhancement of minus-end affinity (Hendershott *et al.*, 2014). Newly polymerized microtubule minus ends should interact with other CAMSAP3 molecules in the cytoplasm via the CKK domain, resulting in microtubules near the minus end decorated with CAMSAP3 over a long range (Jiang *et al*., 2014).

This model is consistent with the correlation between the domain composition of vertebrate CAMSAPs and their ability to decorate and stabilize microtubules. Previous truncation studies have shown that the D2 domain of CAMSAP3 and the MBD in CAMSAP2/3 preferentially bind to GMPCPP-MT over GDP-MT, implying that these regions recognize the expanded lattice (Jiang *et al.*, 2014; Atherton *et al.*, 2017). Similar to the number of regions showing this preference, the microtubule stabilizing effect is higher for CAMSAP3 than CAMSAP2. Also, our model can explain why CAMSAP1, which does not have any region with a high affinity for the expanded lattice, barely affects microtubule stability (Fig. 6B). Thus, the number of regions that prefer the expanded lattice is apparently proportional to the microtubule stabilization effect (Jiang *et al*., 2014; Hendershott *et al*., 2014). In this study, we focus on the D2 region of CAMSAP3 due to difficulty in expressing the MBD in soluble fractions in our system. Future analysis of the MBD together with mutational and swapping analyses of these regions will strengthen our model and provide a comprehensive understanding of the roles of the MBD and D2 regions.

Overall, we demonstrated that the D2 region of CAMSAP3 has two functions: to identify the expanded microtubule lattice (Fig. 1–3) and to expand the compact lattice of GDP-MT (Fig. 4, 5). Both of these functions

are common with the motor protein KIF5C and mitosis regulator TPX2. If we assume that the "reading" and "writing" codes on the lattice are correlated, there is a trade-off between the binding specificity of the proteins and their effectiveness at expanding the lattice. If the specificity is low (low reading ability), like in the case of KIF5C, the protein can spontaneously bind to the compacted lattice well, but the resulting expansion is small (low writing ability). Indeed, KIF5C expands the lattice by only ~1% (Shima *et al*., 2018; Peet *et al*., 2018), whereas D2 expands it by ~3% (Fig. 4C). On the contrary, proteins with high specificity, like TPX2 and D2, are expected to expand the lattice longer (high writing ability) but do not bind well on a compact lattice because of the higher specificity for the expanded condition. Therefore, these highly specific proteins require another mechanism to recruit proteins on a compacted lattice before the expansion occurs. As for TPX2, recent light and electron microscopy studies have shown that it is locally concentrated on microtubules by liquid-liquid phase separation and Rayleigh instability (King and Petry, 2020; Setru *et al.*, 2021). As for D2, the CKK domain in the same CAMSAP3 molecule is most likely concentrated at the microtubule minus end (Fig. 6A). Thus, the "reading" and "writing" abilities of these proteins may have been evolutionarily optimized according to their protein structure, binding partners and cellular distribution and function.

Although we have viewed the microtubule structure as either an expanded or compact lattice, the structure is more complex. Contrary to KIF5C-binding, the lattice expansion triggered by D2-binding was not meta-stable, but returned to the original status immediately after D2 dissociation (Fig. 4C). Notably, KIF5C-induced expansion lasts longer even though the relative expansion rate is less than that induced by D2, highlighting the differences in KIF5C- and D2-induced expanded lattices. There is also an inconsistency in that D2 binding GMPCPP-MT was enhanced by KIF5C pre-treatment (Fig. 3) even though KIF5C does not expand the lattice of GMPCPP-MT further (Shima *et al*., 2018). Future structural studies on D2-coated microtubules and comparisons with the structure of KIF5C-bound GDP-MT (Shima *et al*., 2018) will reveal the structural diversity of microtubules with expanded lattices and explain what causes these differences.

Methods

1. Protein purification and labeling

Tubulin was purified from porcine brains by polymerization/depolymerization cycles in high molarity buffer as described previously (Castoldi and Popov, 2003). For GTP-bound tubulin, polymerization/depolymerization was repeated for three cycles. In the final cycle, tubulin was depolymerized in PEM (100 mM PIPES-KOH, 1 mM EGTA, and 2 mM $MgSO_4$, pH 6.9 supplemented with 0.1 mM GTP, snap-frozen and stored in liquid nitrogen. To prepare GMPCPP-bound tubulin, two cycles were conducted in the same way as GTP-bound tubulin, and purified tubulin was subsequently subjected to two polymerization/depolymerization cycles using 0.1 mM GMPCPP (NU-405L; Jena Bioscience) instead of 1 mM GTP. In the final cycle, tubulin was depolymerized in PEM containing 0.1 mM GMPCPP and stored in the same way as GTP-bound tubulin.

Fluorescently labeled tubulin and biotinylated tubulin were prepared by adding Alexa Fluor 488 NHS ester (A20000; Thermo Fisher), Sulfo-Cy5 NHS Ester (13320; Lumiprobe) or Sulfo-Cy5 NHS Ester (13320; Lumiprobe) dissolved in DMSO to polymerize microtubules. Unreacted labels were removed by two dilutions and ultracentrifugation of the microtubules. Labeled tubulin samples were mixed with intact tubulin at the indicated labeling rates, snap-frozen and stored in liquid nitrogen.

The human CAMSAP3 gene was bought from Riken (GNP Clone IRAL050D13) and cloned into pET11a plasmid vector. Plasmids were transformed into Rosetta II competent cells (71397; Novagen) and incubated in 2x YT medium (16 g/L bacto-tryptone, 10 g/L yeast extract, 5 g/L NaCl) supplemented with 10 µg/mL ampicillin in a 37°C shaker until the OD600 reached ~0.6. Protein expression was induced by a 5.5-hour incubation at 18°C in the presence of 0.5 mM IPTG. Bacteria were collected, snap-frozen in liquid nitrogen and stored at -80°C. For protein purification, bacteria pellets were resuspended in lysis buffer (50 mM Tris-HCl, 500 mM NaCl, 10 mM imidazole, pH 8.0) supplemented with protease inhibitor cocktail (1 mM 4-(2-aminoethyl) benzenesulfonil fluoride, 20 µM Leupeptin, 8.7 µM Pepstatin, and 1 mM N-p-tosyl-L-argininie-methyl ester), sonicated and pelleted by centrifugation at 18,000 x g for 10 min. D2-mCherry was retrieved from the supernatant using its 6x Histidine tag by Ni-NTA agarose resin (141-09764; FUJIFILM). The resin was washed twice with 1.5 column volumes of wash buffer A (50 mM Tris-HCl, 500 mM NaCl, 100 mM imidazole, pH 8.0), twice with 1.5 column volumes of wash buffer B (50 mM Tris-HCl, 500 mM NaCl, 150 mM imidazole, pH 8.0) and lastly once with wash buffer C (50 mM Tris-HCl, 500 mM NaCl, 300 mM imidazole, pH 8.0). The second fraction from the washout using wash buffer B was concentrated and mixed with BRB30 (30 mM PIPES-KOH, 1 mM EGTA, 2mM $MgSO_4$, pH 7.0) using a 30-kDa-cutoff centrifugal filter (UFC503096; Merck). Finally, D2-mCherry solution was snap-frozen with liquid nitrogen and stored at -80°C.

KIF5C (residues 1–411) was purified from the *E coli* recombinant protein purification system. Mouse KIF5C gene was cloned into pET11a plasmid with 6xHis-tag inserted in the N-terminal end. Plasmids were first transformed into Rosseta II competent cells and incubated in 2x YT medium supplemented with 10 µg/mL ampicillin and 10 µg/mL Chloramphenicol in a 37°C shaker until the OD600 reached 0.36. Protein expression was induced by a 14-hour incubation at 18°C in the presence of 0.25 mM IPTG. Bacteria were resuspended in lysis buffer (PEM, 150 mM NaCl, 10 mM imidazole, pH 6.9, supplemented with protease inhibitor cocktail), sonicated and pelleted by centrifugation. KIF5C was incubated with Ni-NTA agarose resin and washed with

1.5 column volumes of wash buffer A (PEM, 150 mM NaCl, 100 mM imidazole, pH 6.9) and twice with 1.5 column volumes of wash buffer B (PEM, 150 mM NaCl, 150 mM imidazole, pH 6.9). KIF5C was eluted from the resin with elution buffer (PEM, 150 mM NaCl, 300 mM imidazole, pH 6.9). The elution fraction was concentrated and buffer-exchanged to BRB80 buffer (80 mM PIPES-KOH, 1 mM EGTA, 2 mM $MgSO_4$, pH 7.3) supplemented with 8% glycerol and 0.5 mM DTT using a 30-kDa-cutoff centrifugal filter (UFC503096; Merck). Finally, KIF5C solution was snap-frozen with liquid nitrogen and stored at -80℃.

2. Preparation for binding assay

A PEG-biotin-coated glass chamber was made by silane coupling and a succinimidyl ester reaction. Cover glasses (C022221S; Matsunami Glass) were first subjected to sonication in 1 N KOH and plasma treatment. Glass surfaces were coated with an amino group by sandwiching N-2-(aminoethyl)-3-aminopropyl-triethoxysilane (KBE-603; Shin-Etsu Chemical) and incubation for 20 min at room temperature. These glasses were washed with deionized water 20 times and then incubated with 200 mg/mL of 0.5%-biotinylated NHS-PEG (ME-050-TS and BI-050-TS; NOF) for 90 min at room temperature. Coated glasses were stuck to each other with 30-µm double-sided tape (5603; Nitto-Denko) to make an ~2-mm wide flowing chamber. The glasses were sealed in a food saver in vacuo and stored at -80℃ until use.

GMPCPP-bound tubulin labeled with Alexa Fluor 488 (2% labeled) and biotin (5% labeled) was incubated at 27℃ for 1 h to promote nucleation, followed by 1 h of polymerization at 37℃. Polymerized microtubule samples were purified by centrifugation at 20,000 x g, 35℃ for 25 min.

The glass chamber was treated as following. First, 1 mg/mL NeutrAvidin was loaded into the chamber and incubated for 2 min to let it bind to biotin molecules covalently connected to the glass surface. The glass surface was subsequently deactivated by adding and incubating with 10x blocking solution (1 mg/mL casein, 1% Pluronic F127) for 2 min. After washing them out with BRB80 containing 25% glycerol, GMPCPP-MT seeds were loaded into the chamber and incubated for 2 min to immobilize microtubules on the glass surface. Unbound microtubules were washed out with BRB80 containing 10x blocking solution and 1 mM GTP. To polymerize GDP-MT from the seeds, 28 µM Cy5-labeled tubulin (labeling rate 2%) in polymerization buffer (BRB80, 2x blocking solution, 1 mM GTP) was applied to the chamber, polymerized for 5 min and terminated by washing free tubulin out with washout buffer (BRB80, 25% glycerol, 2x blocking solution). To completely hydrolyze GTP, the chamber was incubated for more than 30 min before any subsequent experiments.

3. Imaging

Images of *in vitro* assays were acquired using an Eclipse Ti (Nikon) TIRF microscope. The microscope was equipped with a 488 nm laser (Coherent OBIS488-60LS), a 532 nm laser (Coherent OBIS532-20LS), a 640 nm laser (Coherent CUBE640-40), a FF01-390/482/532/640-25 excitation filter (Semrock), a Di01-R405/488/532/635-25x36 dichroic mirror (Opto-line), a FF01-446/510/581/703-25 fluorescence filter (Opto-line), an Apo TIRF 60x/1.49 oil objective lens (Nikon) and a Sona sCMOS camera (Andor). All image acquisitions were managed with Micro-manager (v2.0.0; Edelstein *et al.*, 2014). Imaging was performed at room temperature (23-26℃).

4. Binding assay

D2-mCherry in imaging buffer (BRB80, 25% glycerol 1x blocking solution, 0.1% methylcellulose, 5 mM protocatechuic acid (Pacific Bioscience), 5 mM TSY (Pacific Bioscience), 50 nM protocatechuate-3,4-dioxygenase (Pacific Bioscience)) was applied to the microtubule-immobilized glass chamber (2.). After 5 min of incubation, image acquisition was conducted for all the registered positions. To increase the signal-to-noise ratio, five frames were taken for every position and channel.

For assays in the presence of taxol, D2-mCherry in imaging buffer was supplemented with 20 µM taxol, and images were acquired the same way. Taxol depletion was conducted by exchanging the solution with a sample of same D2 concentration without taxol. Images were taken after a 5-minute incubation.

Since the binding activity of D2 was lost quickly after being thawed (< 1 hour), we prepared new samples every 30 min.

5. Binding assay with KIF5C pre-treatment

During this experiment, 1 µM D2-mCherry in imaging buffer was used for the D2-mCherry samples, and variable concentrations of KIF5C in BRB30 with 25% glycerol was used for the KIF5C pre-treatment. A microtubule-immobilized glass chamber (see 2. Preparation for binding assay) was first incubated with D2-mCherry for 5 min. As a no-pre-treatment control, microtubule-bound D2 was dissociated by a 1-min incubation in high-salt buffer (7.5x PEM, 25% glycerol) followed by washout with BRB80 containing 25% glycerol. Again, D2-mCherry was applied, and the chamber was incubated for 5 min before the image acquisition.

For 0.1, 0.5 and 2.0 µM KIF5C pre-treatment, the incubation/dissociation cycle described below was repeated in the same chamber following the previous image acquisition of D2-bound microtubules. First, D2 was dissociated and washed out by a 1-min incubation in high-salt buffer and a 30-second incubation in BRB80 containing 25% glycerol. Microtubules were subsequently expanded by the addition of KIF5C and incubated for 1 min. Next, KIF5C was dissociated and washed out by a 1-min incubation in high-salt buffer and 30-s incubation in BRB80 containing 25% glycerol. Finally, D2 was applied and incubated for 5 min before the image acquisition.

For the compaction experiment, pre-treatment with 2.0 µM KIF5C was repeated as above except the buffer used for the KIF5C dissociation was ADP buffer (BRB80, 25% glycerol, 1 mM ADP) and not a high-salt buffer.

Note that since this assay takes ~1 h for each run, new D2 samples were prepared between 0 µM and 0.1 µM pre-treatments in addition to the 0.5 µM and 2.0 µM pre-treatments.

6. Data analysis of binding assays

Images acquired by TIRF microscopy were exported as OME-TIF files. Image processing and analysis were done using Python (v3.9.7).

To correct for uneven irradiation by the laser, images were first processed using custom site-package impy (https://github.com/hanjinliu/impy; v2.1.1) as follows. For each channel, all acquired 4D image stacks (stage position, time frame and XY) were projected along the axes of stage positions and frames by the median to

create a 2D background image. This background image was fit to a 2D diagonal Gaussian function:

$$I_{BG}(x,y) = I_0 \exp\left[-(x-\mu_x)^2/2\sigma_x^2 - \left(y-\mu_y\right)^2/2\sigma_y^2\right] + C$$

where I_0 is the peak background intensity, μ_x, μ_y are the peak positions, σ_x, σ_y are the variations of the Gaussian function, and C is a constant. Subsequently, for each separate image slice, intensity values $I(x,y)$ were corrected by:

$$I'(x,y) = I(x,y)/I_{BG}(x,y) \cdot \max(I_{BG}) - \max(I_{BG})$$

to extract the true fluorescence intensity. The corrected image $I'(x,y)$ was averaged by the second to fifth frames and saved as 32-bit floating image stacks in TIF format. The first frame was not used for the analysis because some of them were not in-focus due to the short buffering time after the stage movement.

To remove leakage of the fluorescence intensity between channels, blue-to-green, green-to-blue, red-to-green and green-to-red leakage ratios were determined as follows. The green channel mean intensity along Alexa Fluor 488-labeled microtubules and Cy5-labeled microtubules were measured without D2-mCherry to calculate the blue-to-green and red-to-green leakage. Microtubules saturated with D2 (microtubules equilibrated with 4 μM D2 and 20 μM taxol) were used to measure the blue channel mean intensity along Cy5-labeled microtubules and red channel mean intensity along Alexa Fluor 488-labeled microtubules to calculate green-to-blue and green-to-red leakage. Leakage-corrected images were saved as 32-bit floating image stacks in TIF format.

Average fluorescence intensities along microtubules were quantified using Python image viewer napari (v0.4.16; Sofroniew *et al.*, 2022) and custom plugin napari-filaments (https://github.com/hanjinliu/napari-filaments; v0.2.1). Briefly, fluorescence intensities (Alexa Fluor 488 channel or Cy5 channel) of the non-overlapping regions of microtubules were manually selected and fit to 2D spline curves. For the spline of length L, $\lfloor L \rfloor + 1$ sample points were placed at equal intervals including the edges (i.e., placed for every ~1 pixel), and the intensities were interpolated by cubic interpolation. Average fluorescence intensities were calculated as the average of all interpolated intensities. All statistical tests were calculated using scipy (v1.7.3), statsmodel (v0.13.2; Seabold and Perktold, 2010) or scikit-posthocs (v0.7.0; Terpilowski, 2019).

7. Microtubule expansion assay

Microtubule immobilization was carried out similar to the binding assay (see 4. Binding assay) but slightly modified to fit the expansion assay. After GMPCPP-MT was added, 28 μM Cy5-labeled tubulin (10% labeled) was used for a 15-min polymerization period to lengthen and brighten the microtubules. Subsequently, 8 μM Alexa Fluor 488-labeled tubulin (2% labeled) with 1 mM GMPCPP was loaded into the chamber and polymerized for 20 minutes. Polymerization was terminated by washing free tubulin out with washout buffer. Images were acquired before and after 4 μM D2-mCherry in imaging buffer was added to the chamber followed by the dissociation of D2 by a 1-min incubation in high-salt buffer and washout by imaging buffer for 30 s.

To calculate expansion, a background correction was performed in the same way as the data analysis for the binding assay (see 6. Data analysis of binding assays). Microtubule lengths were measured using napari-filaments as follows. First, the Cy5 channel and Alexa Fluor 488 channel of the image were added with 1:1 weight to create a total intensity image. This image was used for 2D spline fitting as mentioned in the data

analysis of binding assay (see 6. Data analysis of binding assays). Next, the spline curves were clipped at the Cy5-labeled microtubule edges by fitting to the error function:

$$f(x) = \frac{a-b}{2}\left(1 + \mathrm{erf}\left(\frac{x - x_0}{\sqrt{2}\sigma}\right)\right) + b \qquad \left(\mathrm{erf}(x) = \frac{2}{\sqrt{\pi}}\int_0^x e^{-t^2}\,dt\right)$$

The parameters of the error function indicate that intensity increases from b to a, where the inflection point of the intensity change is x_0. Cy5-labeled microtubule lengths were obtained by fragmenting the spline curve into 1024 pieces and summing the lengths of all fragments.

8. Microtubule depolymerization assay

Cy5-labeled GDP-MT (10% labeled) was grown from Alexa Fluor 488-labeled GMPCPP-MT (2% labeled) in the same way as the microtubule expansion assay (see 7. Microtubule expansion assay). After 30-min incubation to hydrolyze GTP completely, the chamber was washed with washout buffer (BRB80, 25% glycerol, 2x blocking solution) with or without 4 µM D2 and incubated for 5 min. Subsequently, glycerol-free imaging buffer (BRB80, 1x blocking solution, 0.1% methylcellulose, 5 mM protocatechuic acid, 5 mM TSY, 50 nM protocatechuate-3,4-dioxygenase) with or without 4 µM D2 was flowed into the chamber, and image acquisition was started immediately. For experiments without D2, images were taken at 0.5-s intervals; for those with D2, images were taken at 5-s intervals.

Instead of building kymographs, we measured the decrease in Cy5 total intensity to quantify the depolymerization rate. Areas that microtubules occupied during depolymerization were manually drawn using max projection as the reference. Total Cy5 intensity in the area was measured for every frame, and the values were converted into length using the ratio of microtubule length to total Cy5 intensity of the first frame. The depolymerization rate was determined by a linear regression of data points that corresponded to microtubule lengths longer than 0.5 µm using the scikit-learn package (v1.0.1; Pedregosa *et al*., 2011). This workflow was applied to all the microtubules independently.

Data availability

All image data sets will be provided upon request.

Acknowledgement

We thank P. Karagiannis (Sofia Science Writing) for proofreading and helpful comments on the manuscript. We also thank the members of the Uemura laboratory for valuable discussions.

Author contributions

Conceptualization, H.L. and T.S.; Data curation, H.L.; Methodology, H.L. and T.S.; Investigation, H.L.; Analysis, H.L.; Supervision, T.S.; Visualization, H.L.; Writing – original draft, H.L.; Writing – review & editing, H.L. and T.S.

Funding and additional information

This work is supported by JSPS KAKENHI (18K06147,19H05379 and 21H00387 to T.S.).

Conflict of interests

The authors declare no conflicts of interest associated with this manuscript.

References

Aher, A., Kok, M., Sharma, A., Rai, A., Olieric, N., Rodriguez-Garcia, R., ... & Akhmanova, A. (2018). CLASP suppresses microtubule catastrophes through a single TOG domain. *Developmental cell*, *46*(1), 40-58.

Ainavarapu SR, Brujic J, Huang HH, Wiita AP, Lu H, Li L, Walther KA, Carrion-Vazquez M, Li H, Fernandez JM. Contour length and refolding rate of a small protein controlled by engineered disulfide bonds. Biophys J. 2007 Jan 1;92(1):225-33. doi: 10.1529/biophysj.106.091561. Epub 2006 Oct 6.

Akhmanova, A., & Steinmetz, M. O. (2019). Microtubule minus-end regulation at a glance. Journal of cell science, 132(11), jcs227850.

Alushin, G. M., Lander, G. C., Kellogg, E. H., Zhang, R., Baker, D., & Nogales, E. (2014). High-resolution microtubule structures reveal the structural transitions in αβ-tubulin upon GTP hydrolysis. Cell, 157(5), 1117-1129.

Atherton, J., Jiang, K., Stangier, M. M., Luo, Y., Hua, S., Houben, K., Van Hooff, J. J. E., Joseph, A. P., Scarabelli, G., Grant, B. J., Roberts, A. J., Topf, M., Steinmetz, M. O., Baldus, M., Moores, C. A., & Akhmanova, A. (2017). A structural model for microtubule minus-end recognition and protection by CAMSAP proteins. Nature Structural and Molecular Biology, 24(11), 931–943.

Atherton, J., Luo, Y., Xiang, S., Yang, C., Rai, A., Jiang, K., ... & Moores, C. A. (2019). Structural determinants of microtubule minus end preference in CAMSAP CKK domains. *Nature communications*, *10*(1), 1-16.

Ayukawa, R., Iwata, S., Imai, H., Kamimura, S., Hayashi, M., Ngo, K. X., ... & Muto, E. (2021). GTP-dependent formation of straight tubulin oligomers leads to microtubule nucleation. *Journal of Cell Biology*, *220*(4).

Caplow, M., Shanks, J., & Ruhlen, R. (1994). How taxol modulates microtubule disassembly. *Journal of Biological Chemistry*, *269*(38), 23399-23402.

Castoldi, M., & Popov, A. V. (2003). Purification of brain tubulin through two cycles of polymerization–depolymerization in a high-molarity buffer. *Protein expression and purification*, *32*(1), 83-88.

Coquand, L., Victoria, G. S., Tata, A., Carpentieri, J. A., Brault, J. B., Guimiot, F., Fraisier, V., & Baffet, A. D. (2021). CAMSAPs organize an acentrosomal microtubule network from basal varicosities in radial glial cells. Journal of Cell Biology, 220(8).

Dent, E. W., & Baas, P. W. (2014). Microtubules in neurons as information carriers. *Journal of neurochemistry*, *129*(2), 235-239.

Dogterom, M., & Koenderink, G. H. (2019). Actin–microtubule crosstalk in cell biology. Nature Reviews Molecular Cell Biology, 20(1), 38-54.

Edelstein, A. D., Tsuchida, M. A., Amodaj, N., Pinkard, H., Vale, R. D., & Stuurman, N. (2014). Advanced methods of microscope control using μManager software. *Journal of biological methods*, *1*(2).

Estévez-Gallego, J., Josa-Prado, F., Ku, S., Buey, R. M., Balaguer, F. A., Prota, A. E., ... & Oliva, M. A. (2020). Structural model for differential cap maturation at growing microtubule ends. *Elife*, *9*, e50155.

Farmer, V., Arpağ, G., Hall, S. L., & Zanic, M. (2021). XMAP215 promotes microtubule catastrophe by disrupting the growing microtubule end. *Journal of Cell Biology*, *220*(10), e202012144.

Feng, C., Thyagarajan, P., Shorey, M., Seebold, D. Y., Weiner, A. T., Albertson, R. M., ... & Rolls, M. M. (2019). Patronin-mediated minus end growth is required for dendritic microtubule polarity. *Journal of Cell Biology*, *218*(7), 2309-2328.

Gadde, S., & Heald, R. (2004). Mechanisms and molecules of the mitotic spindle. Current Biology, 14(18), R797-R805.

Goodson, H. V., & Jonasson, E. M. (2018). Microtubules and microtubule-associated proteins. Cold Spring Harbor perspectives in biology, 10(6), a022608.

Goodwin, S. S., & Vale, R. D. (2010). Patronin regulates the microtubule network by protecting microtubule minus ends. *Cell*, *143*(2), 263-274.

Hendershott, M. C., & Vale, R. D. (2014). Regulation of microtubule minus-end dynamics by CAMSAPs and Patronin. *Proceedings of the National Academy of Sciences*, *111*(16), 5860-5865.

Hyman, A. A., Chrétien, D., Arnal, I., & Wade, R. H. (1995). Structural changes accompanying GTP hydrolysis in microtubules: information from a slowly hydrolyzable analogue guanylyl-(alpha, beta)-methylene-diphosphonate. *The Journal of cell biology*, *128*(1), 117-125.

Imasaki, T., Kikkawa, S., Niwa, S., Saijo-Hamano, Y., Shigematsu, H., Aoyama, K., ... & Nitta, R. (2022). CAMSAP2 organizes a γ-tubulin-independent microtubule nucleation centre through phase separation. *Elife*, *11*, e77365.

Jiang, K., Hua, S., Mohan, R., Grigoriev, I., Yau, K. W., Liu, Q., ... & Akhmanova, A. (2014). Microtubule minus-end stabilization by polymerization-driven CAMSAP deposition. *Developmental cell*, *28*(3), 295-309.

Job, D., Valiron, O., & Oakley, B. (2003). Microtubule nucleation. *Current opinion in cell biology*, *15*(1), 111-117.

Kamimura, S., Fujita, Y., Wada, Y., Yagi, T., & Iwamoto, H. (2016). X-ray fiber diffraction analysis shows dynamic changes in axial tubulin repeats in native microtubules depending on paclitaxel content, temperature and GTP-hydrolysis. *Cytoskeleton*, *73*(3), 131-144.

King, M. R., & Petry, S. (2020). Phase separation of TPX2 enhances and spatially coordinates microtubule nucleation. *Nature communications*, *11*(1), 1-13.

LaFrance, B. J., Roostalu, J., Henkin, G., Greber, B. J., Zhang, R., Normanno, D., ... & Nogales, E. (2022). Structural transitions in the GTP cap visualized by cryo-electron microscopy of catalytically inactive microtubules. *Proceedings of the National Academy of Sciences*, *119*(2), e2114994119.

Li, Y., Edsall, R., Jagtap, P. G., Kingston, D. G., & Bane, S. (2000). Equilibrium studies of a fluorescent paclitaxel derivative binding to microtubules. *Biochemistry*, *39*(3), 616-623.

Meng, W., Mushika, Y., Ichii, T., & Takeichi, M. (2008). Anchorage of microtubule minus ends to adherens junctions regulates epithelial cell-cell contacts. *Cell*, *135*(5), 948-959.

Mitchison, T., & Kirschner, M. (1984). Dynamic instability of microtubule growth. *nature*, *312*(5991), 237-242.

Morikawa, M., Yajima, H., Nitta, R., Inoue, S., Ogura, T., Sato, C., & Hirokawa, N. (2015). X-ray and Cryo-EM structures reveal mutual conformational changes of Kinesin and GTP-state microtubules upon binding. *The EMBO journal*, *34*(9), 1270-1286.

Nakata, T., Niwa, S., Okada, Y., Perez, F., & Hirokawa, N. (2011). Preferential binding of a kinesin-1 motor to GTP-tubulin–rich microtubules underlies polarized vesicle transport. *Journal of Cell Biology*, *194*(2), 245-255.

Pedregosa, F., Varoquaux, G., Gramfort, A., Michel, V., Thirion, B., Grisel, O., ... & Duchesnay, E. (2011). Scikit-learn: Machine learning in Python. *the Journal of machine Learning research*, *12*, 2825-2830.

Peet, D. R., Burroughs, N. J., & Cross, R. A. (2018). Kinesin expands and stabilizes the GDP-microtubule lattice. Nature nanotechnology, 13(5), 386-391.

Pongrakhananon, V., Saito, H., Hiver, S., Abe, T., Shioi, G., Meng, W., & Takeichi, M. (2018). CAMSAP3 maintains neuronal polarity through regulation of microtubule stability. Proceedings of the National Academy of Sciences of the United States of America, 115(39), 9750–9755.

Roostalu, J., Cade, N. I., & Surrey, T. (2015). Complementary activities of TPX2 and chTOG constitute an efficient importin-regulated microtubule nucleation module. *Nature cell biology*, *17*(11), 1422-1434.

Ross, J. L., Santangelo, C. D., Makrides, V., & Fygenson, D. K. (2004). Tau induces cooperative Taxol binding to microtubules. *Proceedings of the National Academy of Sciences*, *101*(35), 12910-12915.

Seabold, S., & Perktold, J. (2010, June). Statsmodels: Econometric and statistical modeling with python. In *Proceedings of the 9th Python in Science Conference* (Vol. 57, No. 61, pp. 10-25080).

Setru, S. U., Gouveia, B., Alfaro-Aco, R., Shaevitz, J. W., Stone, H. A., & Petry, S. (2021). A hydrodynamic instability drives protein droplet formation on microtubules to nucleate branches. *Nature physics*, *17*(4), 493-498.

Shima, T., Morikawa, M., Kaneshiro, J., Kambara, T., Kamimura, S., Yagi, T., ... & Hirokawa, N. (2018). Kinesin-binding–triggered conformation switching of microtubules contributes to polarized transport. Journal of Cell Biology, 217(12), 4164-4183.

Sofroniew, Nicholas, Lambert, Talley, Evans, Kira, Nunez-Iglesias, Juan, Bokota, Grzegorz, Winston, Philip, Peña-Castellanos, Gonzalo, Yamauchi, Kevin, Bussonnier, Matthias, Doncila Pop, Draga, Can Solak, Ahmet, Liu, Ziyang, Wadhwa, Pam, Burt, Alister, Buckley, Genevieve, Sweet, Andrew, Migas, Lukasz, Hilsenstein, Volker, Gaifas, Lorenzo, … McGovern, Abigail. (2022). napari: a multi-dimensional image viewer for Python (v0.4.16). Zenodo. https://doi.org/10.5281/zenodo.6598542

Tanaka, N., Meng, W., Nagae, S., & Takeichi, M. (2012). Nezha/CAMSAP3 and CAMSAP2 cooperate in epithelial-specific organization of noncentrosomal microtubules. *Proceedings of the National Academy of Sciences*, *109*(49), 20029-20034.

Terpilowski, M. A. (2019). scikit-posthocs: Pairwise multiple comparison tests in Python. *Journal of Open Source Software*, *4*(36), 1169.

Toya, M., Kobayashi, S., Kawasaki, M., Shioi, G., Kaneko, M., Ishiuchi, T., Misaki, K., Meng, W., & Takeichi, M. (2016). CAMSAP3 orients the apical-to-basal polarity of microtubule arrays in epithelial cells. Proceedings of the National Academy of Sciences of the United States of America, 113(2), 332–337.

Williamson, T., Gordon-Weeks, P. R., Schachner, M., & Taylor, J. (1996). Microtubule reorganization is obligatory for growth cone turning. Proceedings of the National Academy of Sciences, 93(26), 15221-15226.

Yajima, H., Ogura, T., Nitta, R., Okada, Y., Sato, C., & Hirokawa, N. (2012). Conformational changes in tubulin in GMPCPP and GDP-taxol microtubules observed by cryoelectron microscopy. *Journal of Cell Biology*, *198*(3), 315-322.

Zanic, M., Widlund, P. O., Hyman, A. A., & Howard, J. (2013). Synergy between XMAP215 and EB1 increases microtubule growth rates to physiological levels. *Nature cell biology*, *15*(6), 688-693.

Zhang, R., LaFrance, B., & Nogales, E. (2018). Separating the effects of nucleotide and EB binding on microtubule structure. *Proceedings of the National Academy of Sciences*, *115*(27), E6191-E6200.

Zhang, R., Roostalu, J., Surrey, T., & Nogales, E. (2017). Structural insight into TPX2-stimulated microtubule assembly. *Elife*, *6*, e30959.

Figures

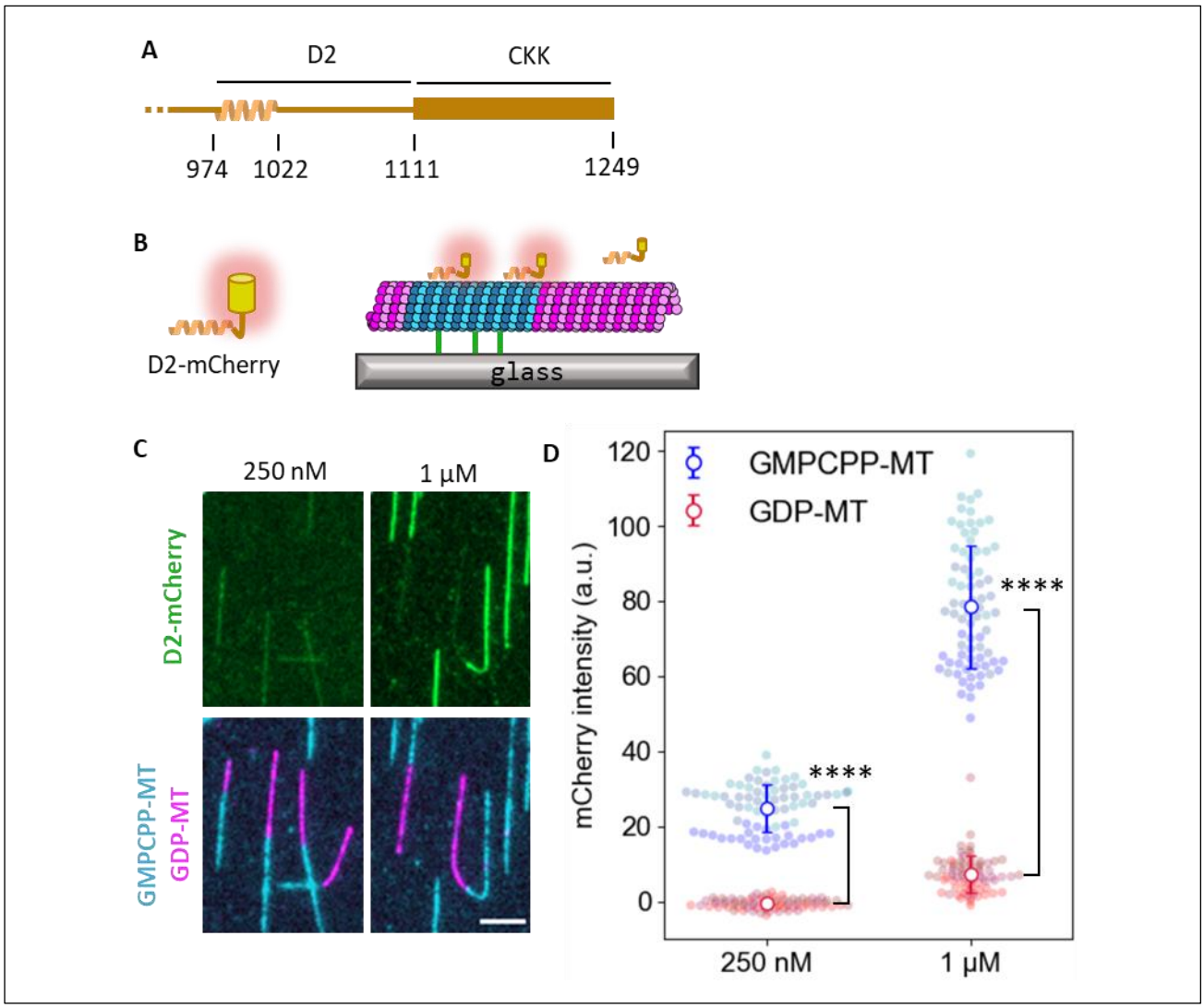

Fig. 1: The D2 region in CAMSAP3 prefers GMPCPP-stabilized microtubules. (A) A schematic of human CAMSAP3 at its C-terminal. (B) A schematic of the TIRF microscopy used in the binding assay. (C) Representative images showing D2 binding to microtubules. Contrasts are set to the same range for each channel. Images after unmixing the fluorescence intensities are shown. Scale bar, 5 μm. 75 GMPCPP-MTs and 75 GDP-MTs from three replicates were analyzed for each D2 concentration. (D) Quantification of the average fluorescence intensity of D2-mCherry along microtubules. Colors represent three replicates. Error bars, S.D. ****: $p < 0.0001$ (Welch's t-test).

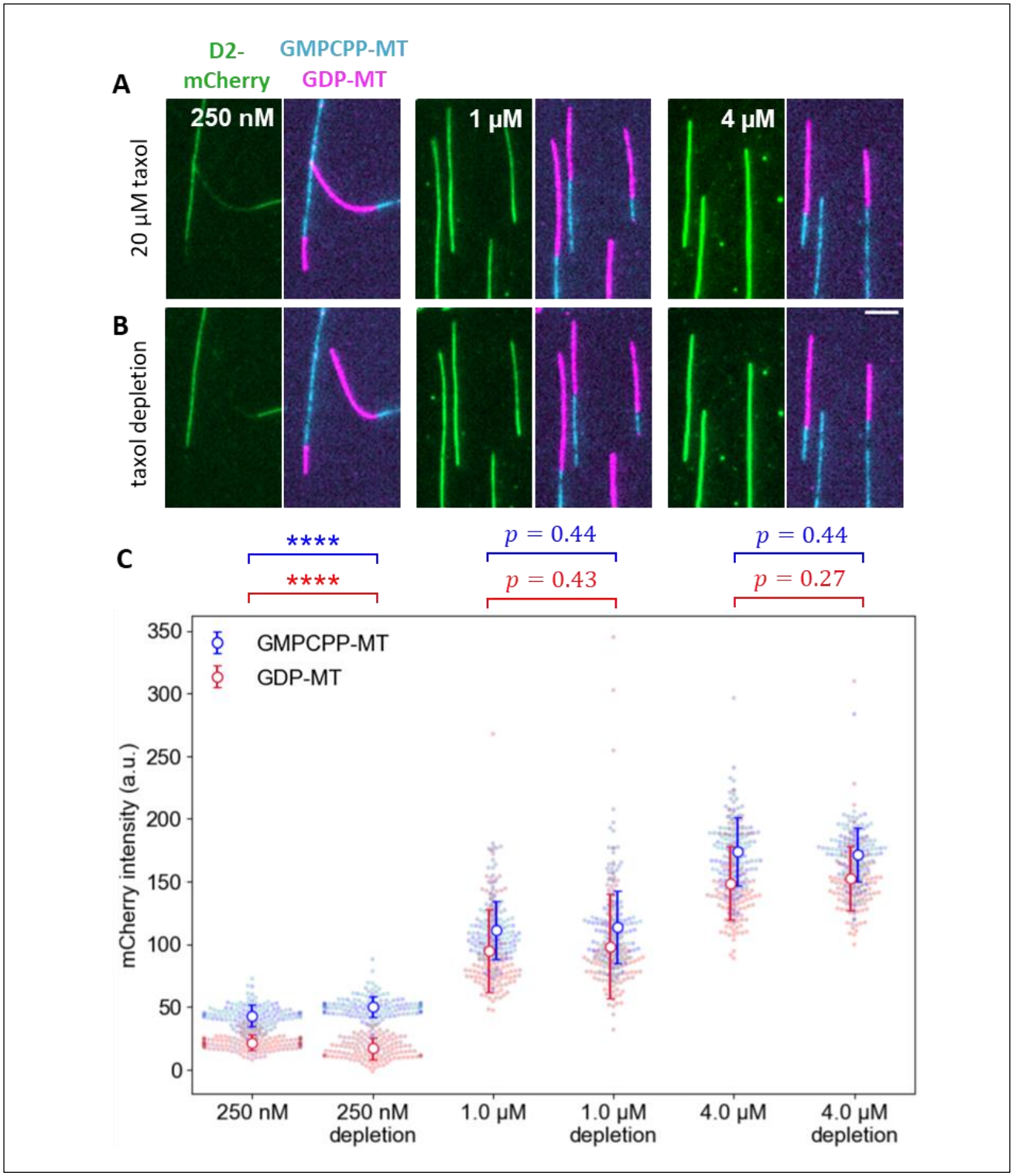
A
D2-mCherry
GMPCPP-MT
GDP-MT
250 nM
1 μM
4 μM
20 μM taxol
B
taxol depletion
C
****
****
p = 0.44
p = 0.43
p = 0.44
p = 0.27
GMPCPP-MT
GDP-MT
mCherry intensity (a.u.)
0
50
100
150
200
250
300
350
250 nM
250 nM depletion
1.0 μM
1.0 μM depletion
4.0 μM
4.0 μM depletion

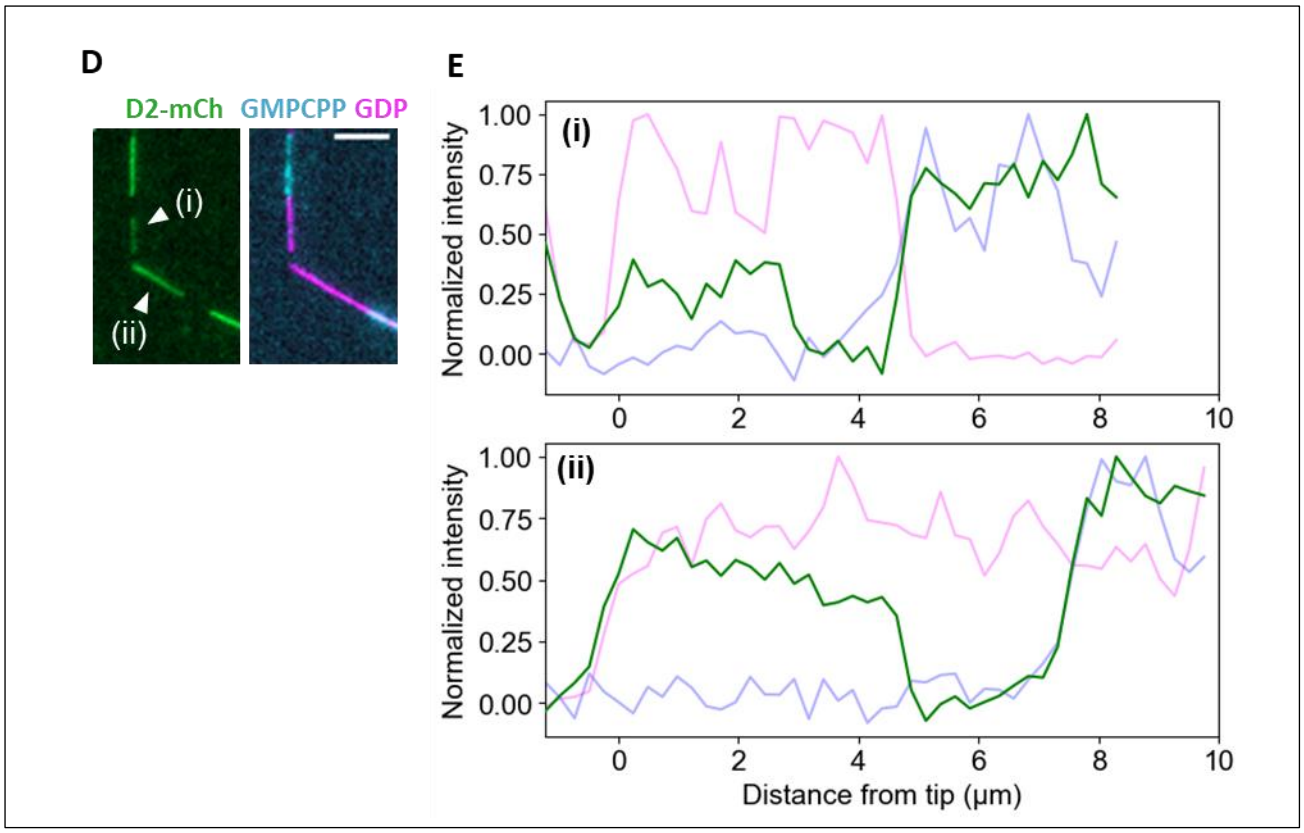

Fig. 2: Affinity of D2 to GDP-MT was enhanced by the addition of taxol. (A, B) Representative images of D2 binding to microtubules in the presence of taxol (A) or after 5-min taxol depletion (B). Contrasts were set to the same range for each channel. Scale bar, 5 μm. (C) Quantification of average fluorescence intensities of D2-mCherry. Error bars, S.D. ****: $p < 0.0001$ (Welch's t-test). For 250 nM D2, Cohen's d after taxol depletion was $d = 0.60$. Sample size of each data set is summarized in Table 1. (D) Representative images of 250 nM D2 forming clusters on GDP-MT after taxol depletion. D2 clusters formed on GDP-MT were marked as (i) and (ii). Scale bar, 5 μm. (E) Line profiles of microtubules in (D) plotted against the distance from the tips.

Table 1: mCherry intensity on microtubules in the taxol-depletion assay.

Condition		mCherry intensity (a. u., mean ± S.D.)		
Microtubule	Taxol	250 nM	1 μM	4 μM
GMPCPP-MT	20 μM	43 ± 9 (n = 130)	112 ± 23 (n = 130)	173 ± 27 (n = 130)
	Depleted	50 ± 8 (n = 130)	114 ± 29 (n = 130)	171 ± 21 (n = 130)
GDP-MT	20 μM	22 ± 6 (n = 130)	95 ± 33 (n = 130)	148 ± 29 (n = 130)
	Depleted	17 ± 8 (n = 130)	98 ± 41 (n = 130)	152 ± 25 (n = 130)

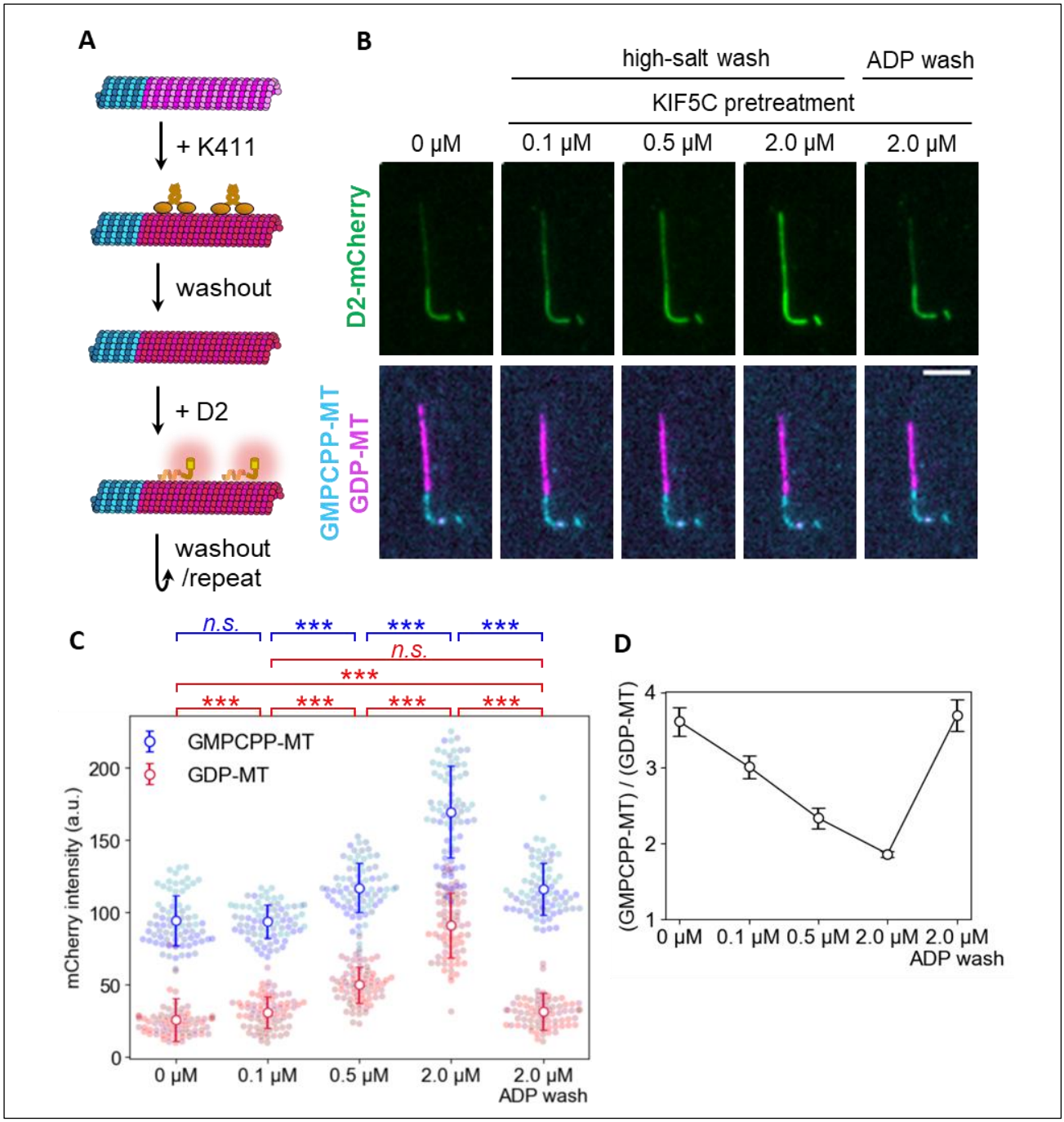

Fig. 3: Microtubule expansion by KIF5C pre-treatment promotes D2-binding. (A) Overview of the KIF5C pre-treatment assay. KIF5C was added to induce microtubule expansion and was washed out before applying D2. (B) Representative images after adding D2. Contrasts are set to the same values for each channel. Scale bar, 5 μm. (C) Quantification of D2-mCherry fluorescence intensity on microtubules. Colors indicate different replicates. Error bars, S.D. ***: $p < 0.001$ (Steel-Dwass test); n.s., not significant. Sample size of each data set is summarized in Table 2. (D) Binding specificity of D2. Specificity was calculated as the mCherry intensity ratio on GMPCPP-MT to that on GDP-MT. Error bars are the standard error predicted by pairs of standard errors in (C) and the error propagation rule.

Table 2: mCherry intensity on microtubules in the kinesin pre-treatment assay.

KIF5C concentration	mCherry intensity (a. u., mean ± S.D.)		GMPCPP/GDP (mean ± S.E.)
	GDP-MT	GMPCPP-MT	
0 μM	26 ± 15 (n = 75)	94 ± 17 (n = 75)	3.61 ± 0.18
0.1 μM	31 ± 11 (n = 75)	93 ± 12 (n = 75)	3.02 ± 0.15
0.5 μM	50 ± 12 (n = 75)	117 ± 17 (n = 75)	2.34 ± 0.14
2 μM	91 ± 22 (n = 75)	170 ± 32 (n = 75)	1.86 ± 0.04
2 μM (ADP wash)	32 ± 13 (n = 75)	116 ± 18 (n = 75)	3.69 ± 0.21

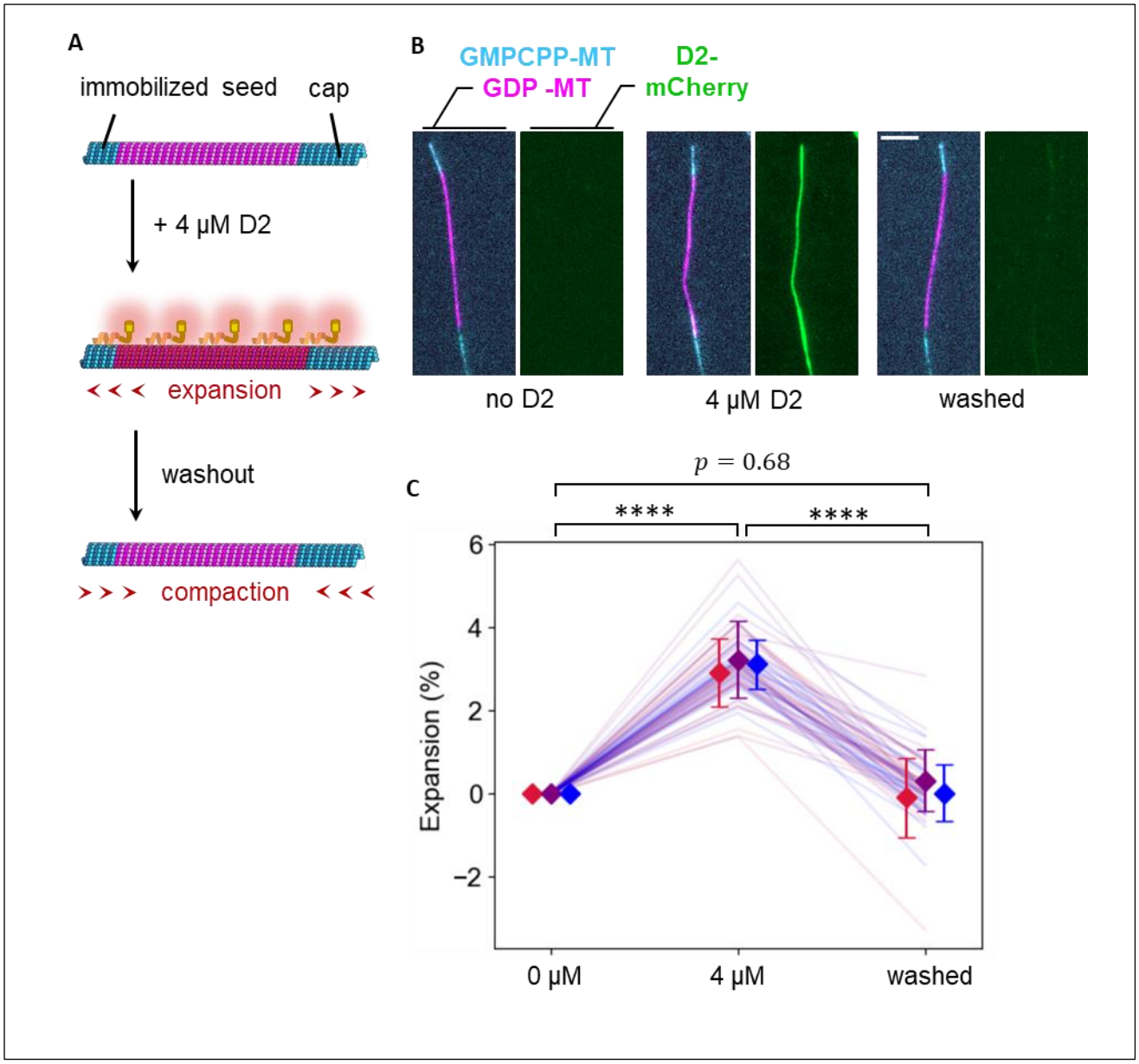

Fig. 4: Microtubule lattice expansion triggered by D2-binding. (A) Schematic illustration of the assay. (B) Representative images during the expansion assay. Red-to-green and green-to-blue fluorescence leakage were unmixed. Scale bar, 5 μm. (C) Quantification of the normalized microtubule length between Alexa Fluor 488-labeled GMPCPP seed and Alexa Fluor 488-labeled GMPCPP-capped microtubules. Microtubule length was calculated by 2D Gaussian fitting of the total intensity and spline fitting in the Cy5 channel. Error bars indicate mean and S.D. of each replicate. ****: $p < 0.0001$ (paired t-test with Bonferroni correction). 64 microtubules from three replicates were analyzed.

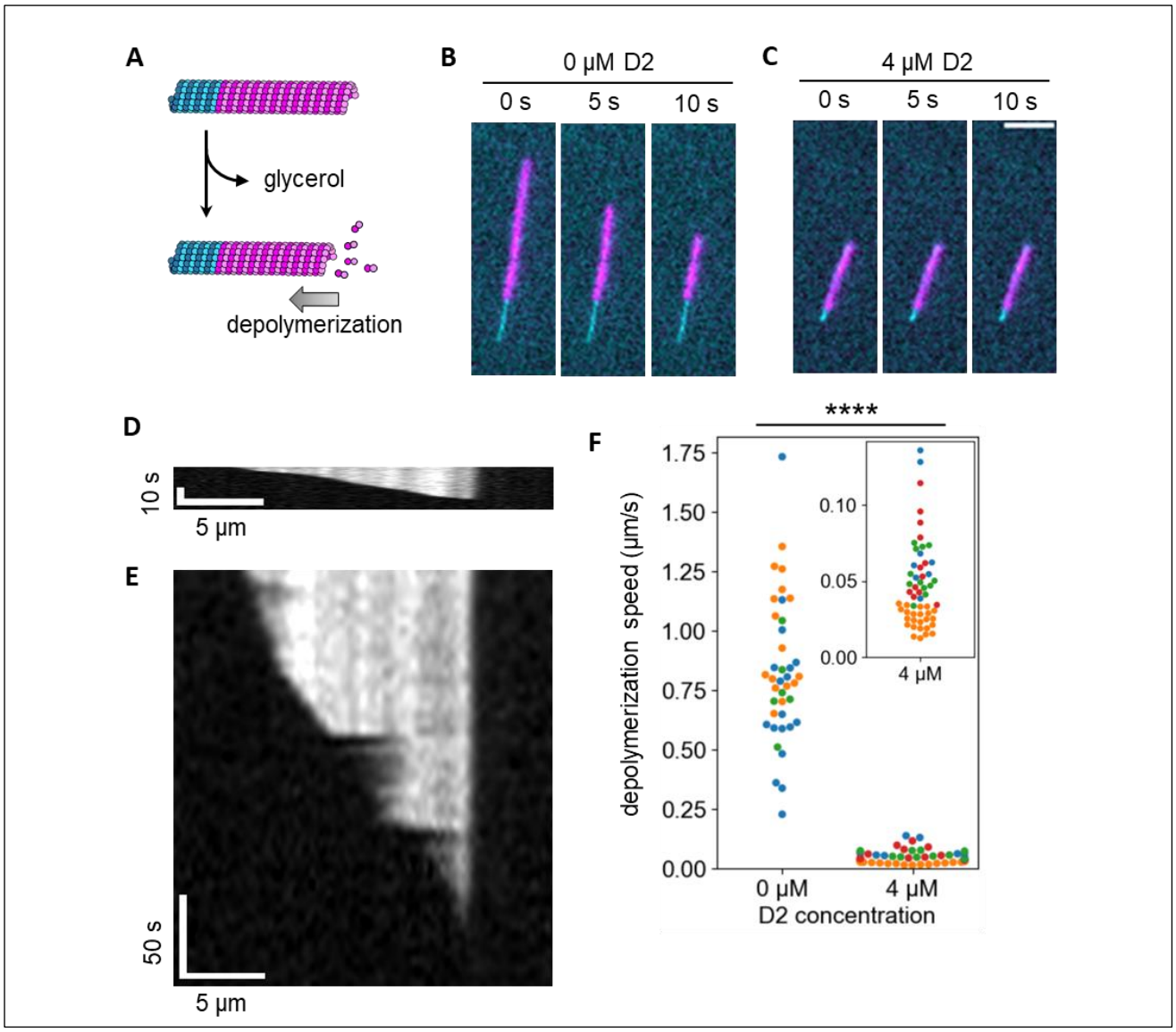

Fig. 5: Microtubule depolymerization was suppressed by D2-binding. (A) Schematic illustration of the assay. Microtubule depolymerization was induced by replacing the buffer with a glycerol-free one. (B, C) Representative frames during depolymerization without D2 (B) or with 4 μM of D2 (C). The cyan channel image (GMPCPP seed) was taken only at the first frame so that the same image was used for three frames. Scale bar, 5 μm. (D, E) Kymographs of depolymerizing microtubules without D2 (D) or with 4 μM D2 (E). Since the images were taken at different time intervals, two kymographs were resized to fit the same time scale. (F) Microtubule depolymerization speed. Different colors represent different replicates. 0 μM: 0.82 ± 0.30 μm/s (mean ± S.D., 40 microtubules, 3 replicates), 4 μM: 0.046 ± 0.028 μm/s (mean ± S.D., 56 microtubules, 4 replicates). ****: $p < 0.0001$ (Welch's t-test).

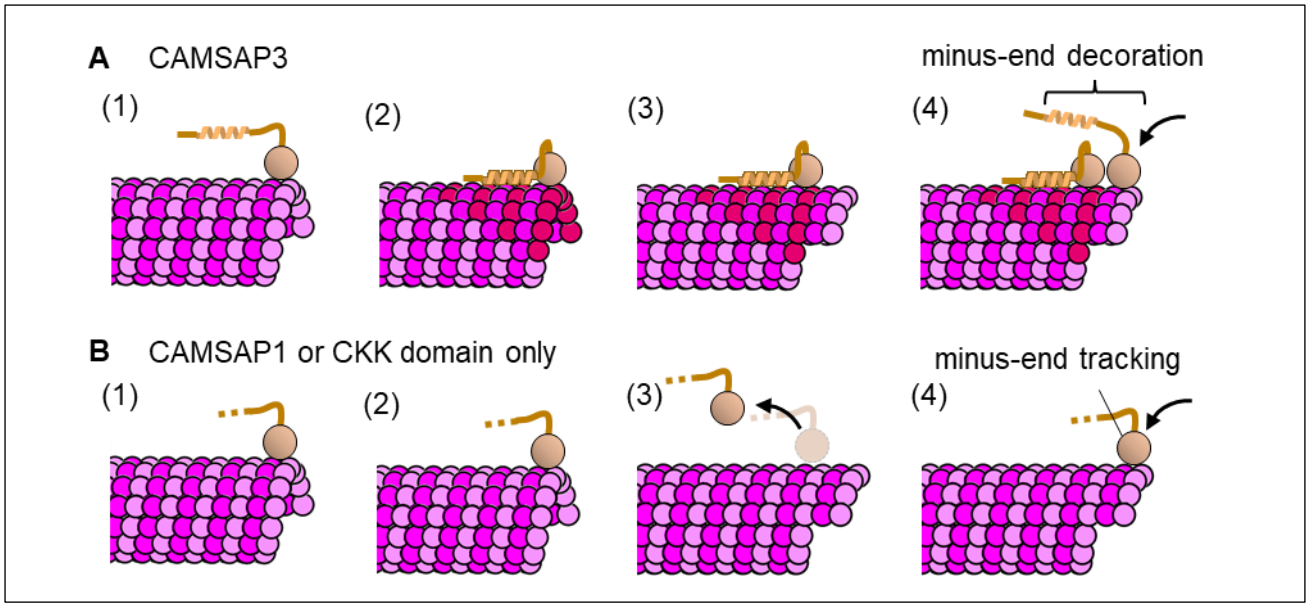

Fig. 6: Model of minus-end decoration and stabilization by CAMSAP3 and comparison with CAMSAP1. (A) CAMSAP3 can specifically bind to the microtubule minus end owing to its CKK domain (1), and the adjacent D2 region expands the microtubule lattice (2). The strong interaction between D2 and expanded microtubule captures CAMSAP3 molecules on the microtubule surface even after the microtubule is polymerized (3). The newly formed minus end provides additional binding sites for other CAMSAP3 proteins (4). This mechanism was observed as minus-end "decoration" under TIRF microscopy. (B) CAMSAP1 can specifically bind to the microtubule minus end (1) but has no effect on the microtubule lattice structure (2). Upon polymerization (3), CAMSAP1 dissociates from the microtubule because where it bound is no longer a minus end. The newly formed minus end is open to CAMSAP1 proteins so that CAMSAP1 appears to be "tracking" the minus end.

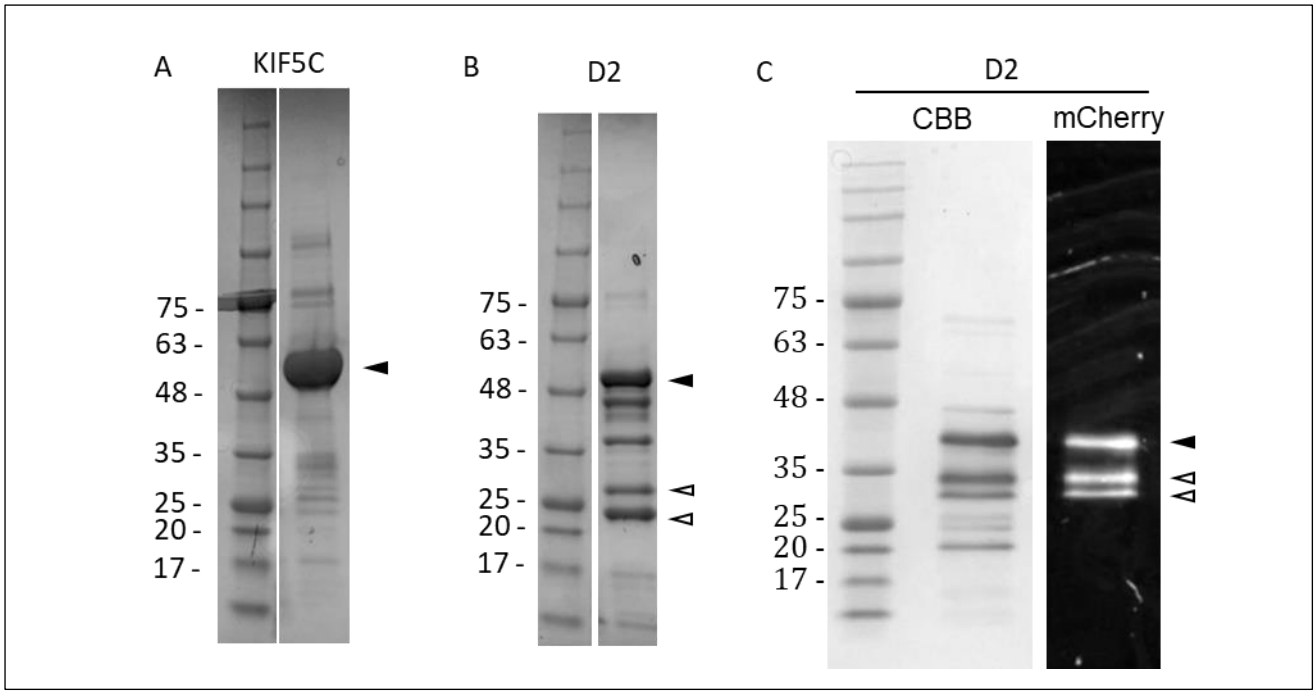

Fig. S1: Pictures of SDS-PAGE gels of purified KIF5C (A), boiled D2-mCherry (B) and non-boiled D2-mCherry (C). The bands indicated by the white arrowheads in the boiled sample (B) are considered fragments of D2-mCherry, because heating by the SDS-PAGE loading buffer splits mCherry. A non-boiled D2 sample (C) was analyzed on SDS-PAGE with CBB staining (left) and mCherry fluorescence (right). The lower mCherry bands (white arrowheads) were attributed to the fragmentation of D2 during the expression and purification processes so that they were not calculated as active fractions. Since purification of the C3 region (D2 + C-terminal CKK domain) of mouse CAMSAP3 also resulted in multiple SDS-PAGE bands in previous work (Fig. S4 of Jiang *et al.*, 2014), we considered this low quality to be inevitable for this protein construct.

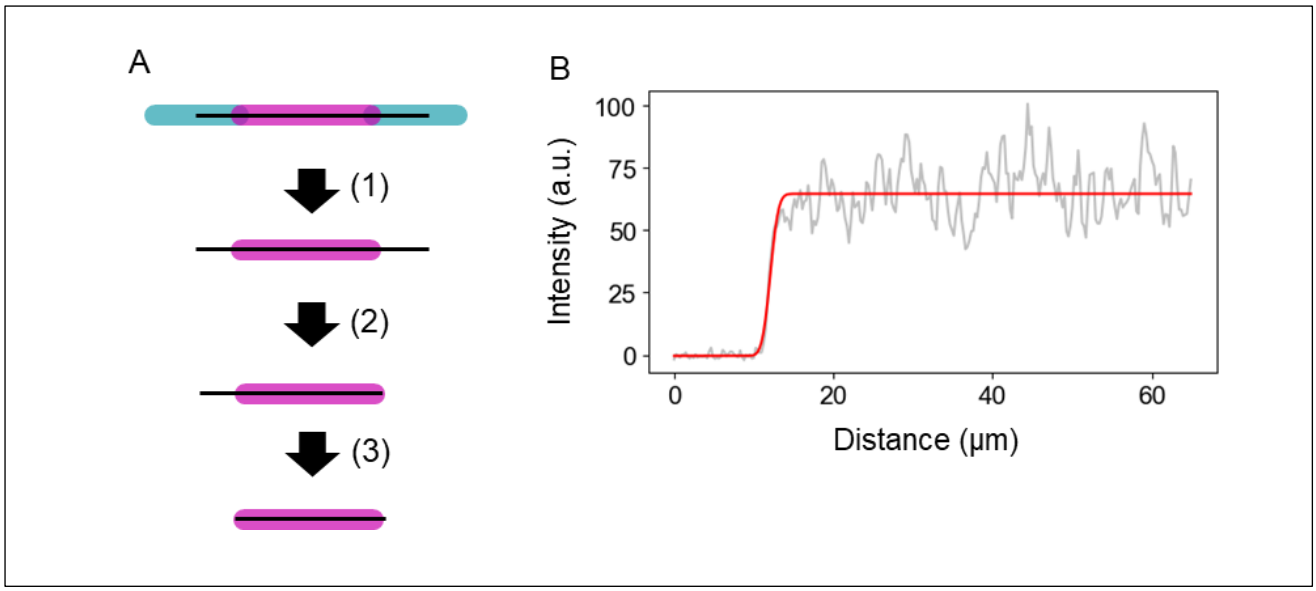

Fig. S2: Illustration of the measurement of microtubule length. (A) The microtubule center line was determined from the total intensity, and the length of the Cy5-labeled microtubule was calculated by fitting the line profile to the error function on each tip. (B) An example of fitting the error function on one tip.

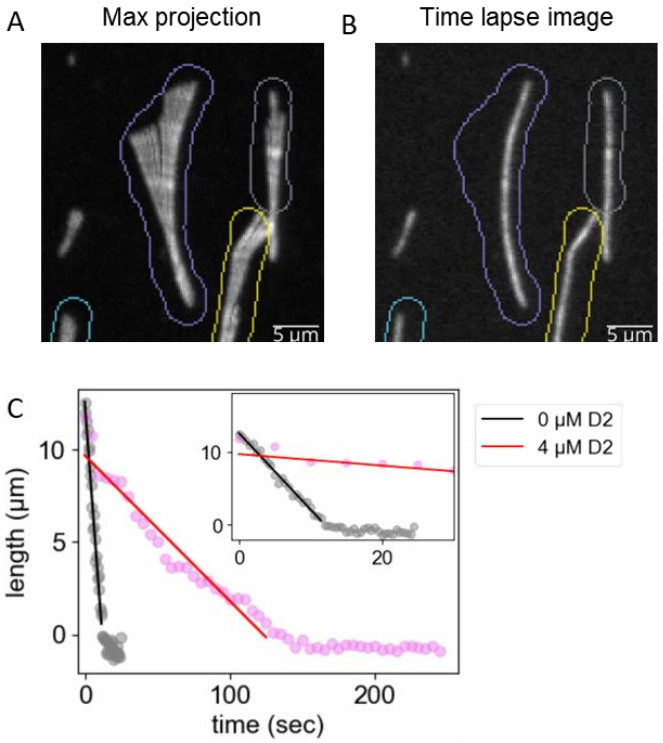

Fig. S3: Quantification of the depolymerization rate of microtubules that were shaking during the image acquisition. (A) Image labels that enclose a microtubule were manually drawn. Colored pixels are the contours of labels. Different color indicates different labels. (B) Overlay of the label contour and time lapse image at $t = 0$. (C) Representative plots of the microtubule length against the imaging time and corresponding results of the linear regression. Length was calculated by associating the fluorescence intensity and microtubule length at $t = 0$.